# **The Formation Mechanism and Suppression Strategies of Spatter in Pulsed Gas Metal Arc Welding for Titanium Alloy**

The mechanism underlying spatter formation and effective strategies to suppress spatter were explored

BY Z. ZHENG, S. WU, L. FAN, H. WU, AND F. CHENG

#### **Abstract**

The GMAW process for titanium alloy is not commonly applied within the industry due to the occurrence of severe spatter. This research endeavors to elucidate the mechanism underlying spatter formation and explore efficacious strategies to suppress spatter. The experimental results demonstrated the existence of two distinct spatter types: large and small spatter particles. The highspeed images and synchronous electrical signals were utilized for determining the spatter formation mechanism, with force analysis serving to mutually validate the inferences. The large spatter particles originated from the whole transitional molten droplet as it descended within the arc space, while the small spatter particles were formed by the partial transitional molten droplet as it contacted the weld pool. The cathode jet force accounted for the formation of large spatter particles, whereas the electromagnetic force was responsible for the small spatter particles. To suppress spatter, increasing detachment current and decreasing pulsing frequency were employed. Consequently, the spatter rate witnessed a remarkable decrease from 14.00% to 3.33% with a progressive increment in detachment current from 100 A to 300 A, and a corresponding decline from 12.67% to 1.33% upon decrementing the pulsing frequency from 90 Hz to 50 Hz. This research suggests that a judicious increase in the detachment current can effectively decrease the spatter rate while concurrently preserving welding efficiency.

# **Keywords**

- Titanium Alloy
- GMAW-P
- Weld Spatter
- Cathode Jet
- Droplet Transfer

#### Introduction

Titanium alloy possesses excellent integrative properties, such as low density, high strength, and remarkable corrosion resistance, rendering it extensively applied in aerospace, automotive, and marine industries (Refs. 1-3). As the demand for large and complex titanium alloy structural components continues to rise in these domains, the necessity for advanced welding techniques has become increasingly pressing. Even though plasma arc welding (PAW) enables the attainment of superior penetration depth (Refs. 4, 5), its implementation encounters challenges when confronted with numerous angular joints due to the intricacy of the welding torch. While gas tungsten arc welding (GTAW) can accommodate the welding of complex structures, its efficiency is considerably hindered by the indirect heating of the filler wire (Refs. 6, 7). Conversely, gas metal arc welding (GMAW) not only exhibits adaptability to complex welding paths but also offers high welding efficiency (Ref. 8), thus positioning itself as a promising welding technique for the fabrication of large and complex titanium alloy structural components.

The GMAW process for titanium alloy is not commonly applied within the industry due to the occurrence of severe spatter resulting from the cathode jet phenomenon (Refs. 6, 7). According to the theory of arc physics, electron emission behavior is typically classified into thermionic emission and field emission, with most materials displaying a dominant preference for either one. However, the level of these two mechanisms in titanium alloy is equally matched owing to

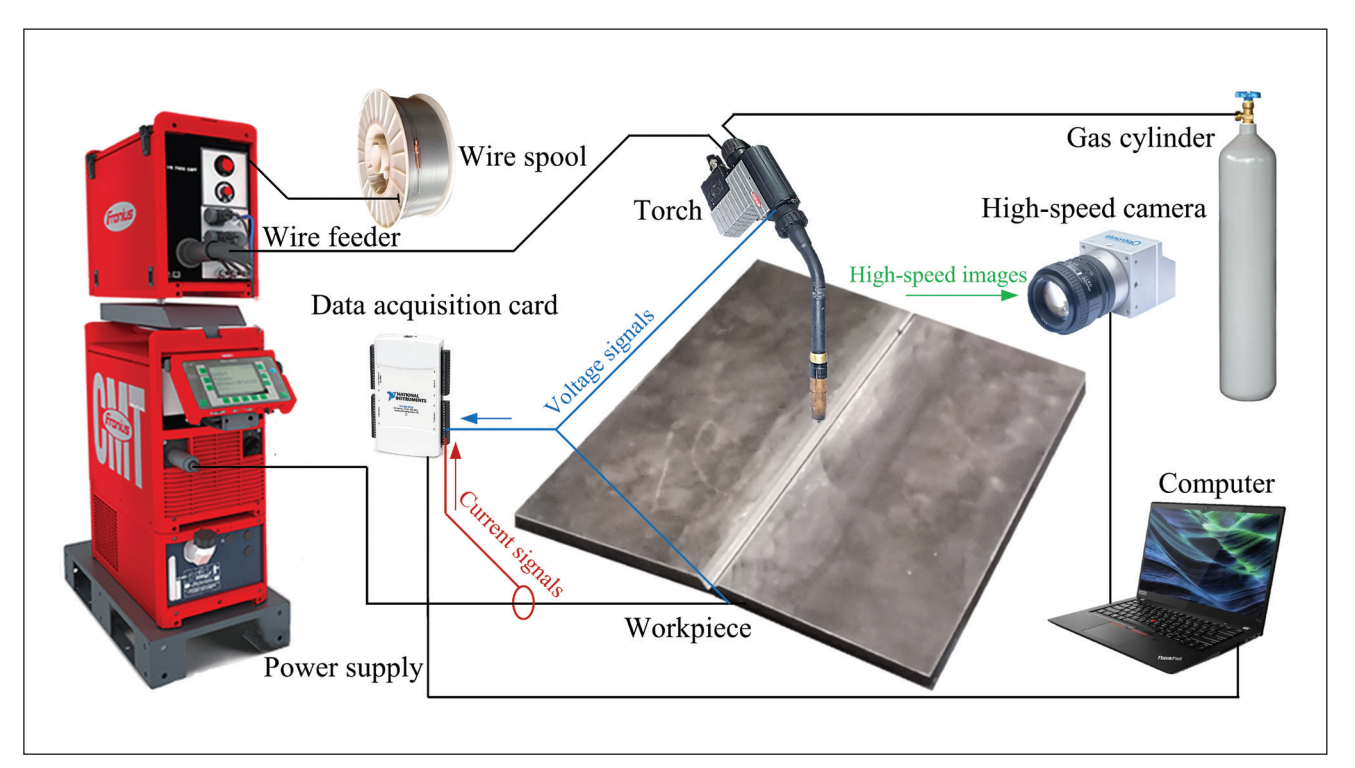


Fig. 1 — The experimental platform built for the GMAW-P process.

the intermediate magnitudes of its physical properties (e.g., boiling temperature, work function, and emissivity) (Ref. 9). This leads to the cathode spot no longer exhibiting irregular jumping behavior but rather becoming fixed at a specific position to emit electrons intensively. Thereby, the originally dispersed electron flow becomes concentrated notably, leading to the formation of a luminous and forceful cathode jet in the opposite direction of the transitional droplets (Refs. 10, 11). As the transitional droplets contact the weld pool, the cathode spot will undergo directional jumping from the weld pool to the apex of the droplets, resulting in the reformation of the cathode jet at a new origin (Ref. 12). During this process, due to the electromagnetic constriction effect causing mutual attraction between current lines, the large current flowing through the unincorporated droplets induces a strong electromagnetic force. This force will expel a portion of the droplets from the weld pool, giving rise to the occurrence of severe spatter and irregular bead formation. The aforementioned elucidates the mechanism underlying the formation of small spatter particles. Furthermore, this research has uncovered a distinct type of spatter, namely large spatter particles, characterized by a different formation mechanism from that of small spatter particles. A detailed description of the formation mechanism pertaining to large spatter particles will be provided in subsequent sections.

To reduce the spatter rate in the GMAW process for titanium alloy, researchers have introduced the laser-GMA hybrid welding technology. Denney et al. (Ref. 13) and Li et al. (Ref. 14) have shown that by controlling high-power laser irradiation (higher than 1 kW) at the leading edge of the weld pool, the temperature at the front of the weld

pool can be raised higher than that of the droplets. This promoted a relatively fixed behavior of the cathode spot without experiencing directional jumping, resulting in significant suppression of spatter formation. Moreover, Denney et al. (Ref. 15) have demonstrated that even a low-power laser (200 W) can also effectively restrain the jumping of the cathode spot, provided it is meticulously controlled. Nevertheless, it should be noted that laser-GMA hybrid welding imposes stringent requirements on precision, inevitably adding complexity to the welding process, and the inherent trade-off between cost and efficiency cannot be disregarded.

Waveform control strategies have also been extensively investigated to reduce the spatter rate. Zhang et al. (Ref. 16) proposed an active control method based on pulsed gas metal arc welding (GMAW-P), which involves the rapid output of a detaching pulse immediately after the exciting pulse ends. This enabled the molten droplets to quickly enter the weld pool under the combination of the increased electromagnetic force and the downward momentum, thus achieving a stable one droplet per pulse (ODPP) metal transfer mode. Sun et al. (Ref. 17) and Zhou et al. (Ref. 18) introduced cold metal transfer (CMT), a modified GMAW process that controls the current drop and wire retraction during the short circuit transfer. This ensured the smooth transfer of molten droplets under the action of surface tension, resulting in the fabrication of well-formed Ti-6Al-4V components. Moreover, Lee et al. (Ref. 19) optimized the detachment current based on the CMT technique, facilitating rapid necking fracture of the molten droplets, thereby enhancing the stability of short circuit transfer. Although these strategies offer high efficiency and quality, the active

Table 1 — The Measured Compositions of the Workpiece and Feedstock (wt-%)											
	Al	٧	Fe	Мо	Ni	Si	С	N	0	Ti	
Work- piece	4.66	0.42	0.025	1.75	0.006	0.12	_	_	-	Bal.	
Feed- stock	5.68	3.72	0.075	_	_		0.015	0.13	0.029	Bal.	

Table 2 — The Processing Parameters Used for GMAW-P Process.										
Group	Base current	Pulsing current	Detachment time	Detachment current	Pulsing frequency					
1-5 6-10	50 A	350 A	1 ms	100, 150, 200, 250, 300 A 200 A	70 Hz 50, 60, 70, 80, 90 Hz					

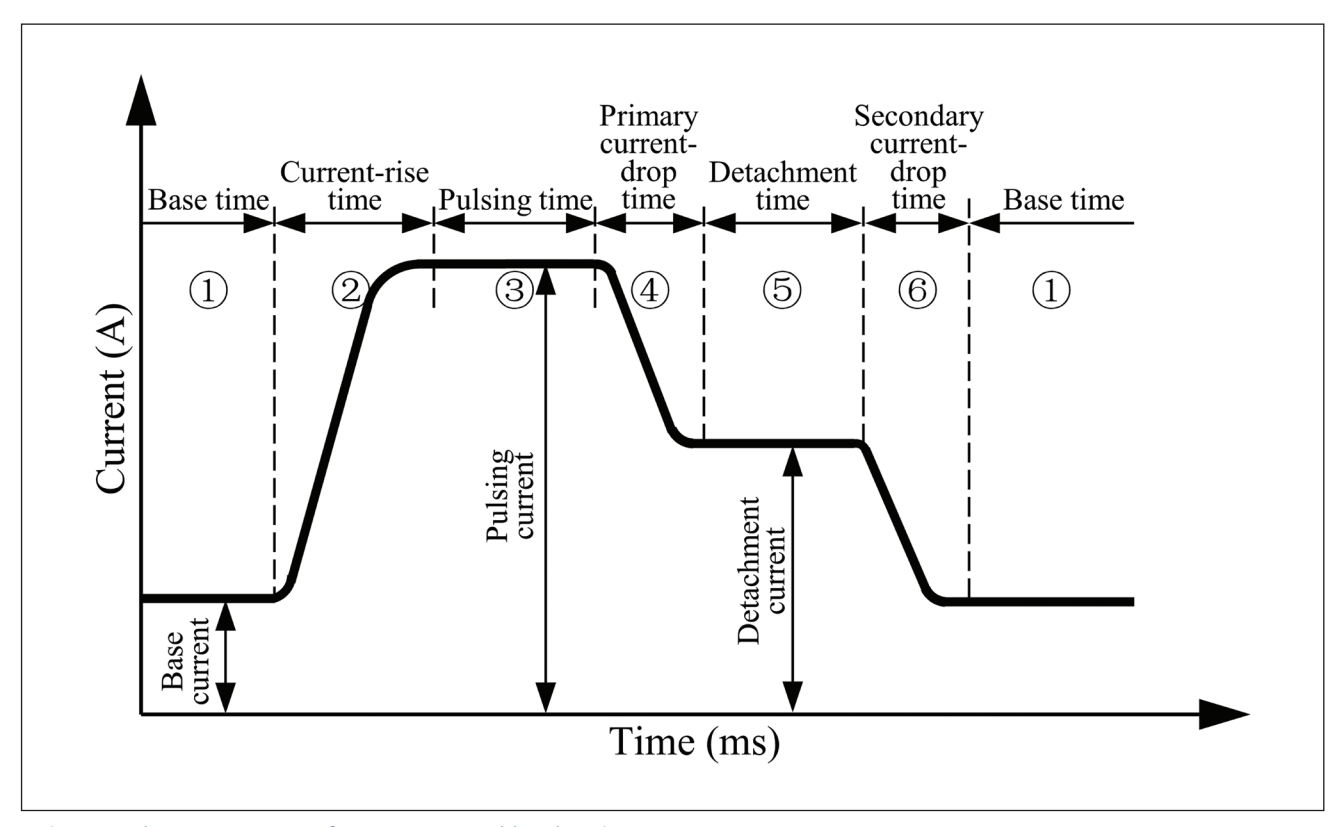


Fig. 2 — The current waveform generated by the Titan RT50.

control method necessitates rapid and precise closed-loop control techniques, and the limited penetration depth of the CMT restricts its application in thick plate welding.

This research endeavors to elucidate the mechanism underlying spatter formation and explore efficacious strategies to suppress spatter in the GMAW-P process for thick titanium alloy plates. The experimental results demonstrated the existence of two distinct spatter types: large and small spatter particles. The high-speed images and synchronous

electrical signals were utilized for determining the spatter formation mechanism, with force analysis serving to mutually validate the inferences. The waveform control strategy was implemented to suppress the spatter by increasing the detachment current coupled with decreasing the pulsing frequency. The spatter rate was quantified to evaluate the efficacy of the waveform control strategy in suppressing spatter formation.

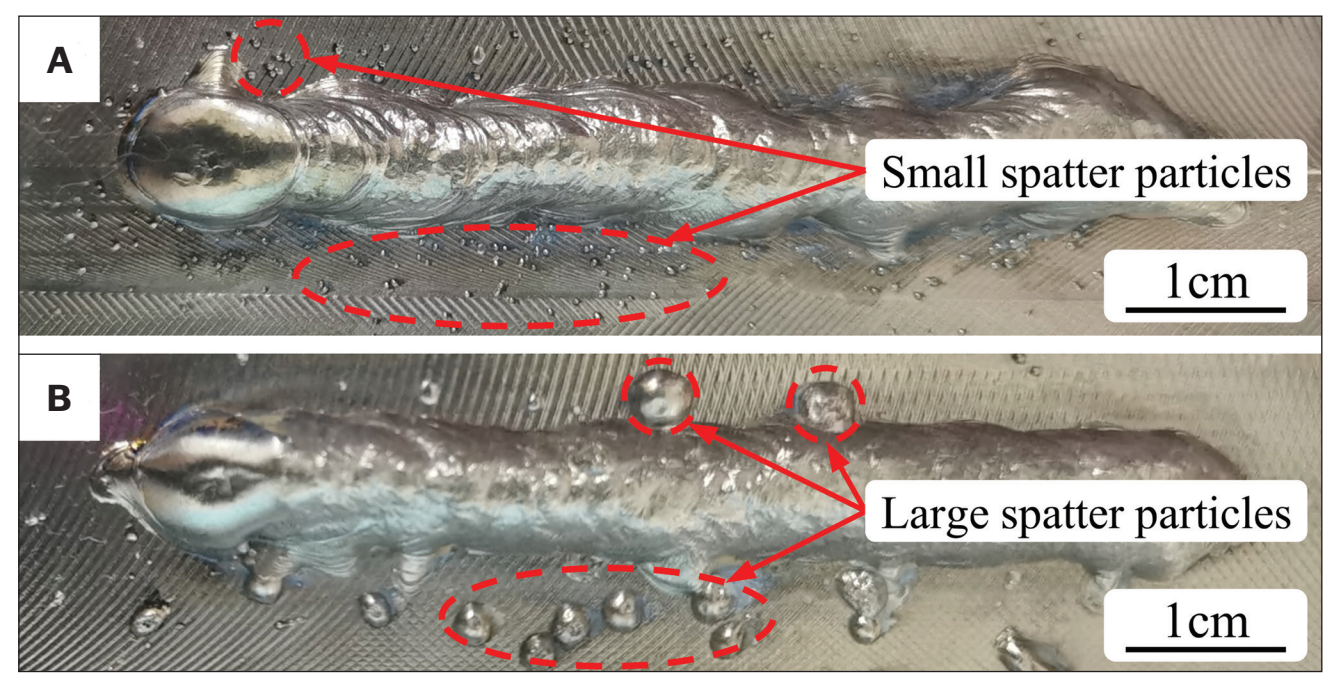


Fig. 3 - A - Small spatter particles; B - large spatter particles on the weld surface.

# **Experiments**

# **Experimental Platform**

The experimental platform is depicted in Fig. 1. The Ti-Al-Mo titanium alloy plate with a thickness of 15.0 mm (0.590 in.) and the Ti-6Al-4V wire with a diameter of 1.2 mm (0.047 in.) were utilized as the workpiece and consumable feedstock, respectively. The measured compositions of these materials are detailed in Table 1. Argon gas with a purity level of 99.99% served as the shielding gas at a flow rate of 18 L (4.755 gal)/min. A six-axis robot arm (ABB IRB 2600, Switzerland) and a welding power supply (Fronius CMT Advanced 4000R, Austria) were employed to conduct the experiments. A high-speed camera (Cylone-2-2000-M, Germany) with a sample rate of 3k frames per second was utilized to capture the droplet transfer behavior. A data acquisition card (NI USB-6218, America) with a sample rate of 10k pulses per second was utilized to synchronously record the current and voltage data.

#### **Experimental Method**

The Titan-RT50, a specialized characteristic curve tailored for welding titanium alloys, was used to conduct the experiments. The current waveform generated by the Titan-RT50 is visually depicted in Fig. 2, while the specific details of the waveform employed in the experiments are presented in Table 2. The current waveform comprises six distinct stages: ① base current, ② current-rise, ③ pulsing current, ④ primary current-drop, ⑤ detachment current, and ⑥ secondary current-drop. During the ideal droplet transfer process, the droplet undergoes slight growth in stage ①, followed by rapid expansion in stage ②, then reaching its critical volume in stage

 $\ \ \,$  $\ \,$  $\ \ \,$  $\ \ \,$  $\ \,$  $\ \ \,$  $\ \ \,$  $\ \ \,$  $\ \ \,$  $\ \ \,$  $\ \ \,$  $\ \ \,$  $\ \ \,$  $\ \ \,$  $\ \ \,$  $\ \ \,$  $\ \ \,$  $\ \ \,$  $\ \ \,$  $\ \ \,$  $\ \,$  $\ \,$  $\ \,$  $\ \,$  $\ \,$  $\ \,$  $\ \,$ 

The workpiece underwent surface grinding to meticulously eliminate the surface oxide film less than 1 hour before the commencement of experiments. The direct current electrode positive (DCEP), which has a cathode-cleaning effect, was employed to prevent oxygen contamination. The experiments were conducted at a torch travel speed of 0.3 m (0.984 ft)/ min and a wire feed speed of 4.7 m (15.420 ft)/min. Two sets of high-speed images were captured for each experimental group. One set employed a xenon lamp as the backlighting to depict the droplet transfer behavior, while the other set, without a xenon lamp, provided a clear visualization of the impingement of the cathode jet on the droplet. The spatter rate was calculated by quantifying the number of spatter particles in 150 droplets, serving as a quantitative measure to assess the effectiveness of the waveform control strategy in suppressing the spatter.

#### Results

In comparison to steel and aluminum, titanium alloy exhibits higher surface tension, requiring a greater amount of energy to facilitate the necking and fracturing phenomena during droplet transfer. The specifically tailored current waveform generated by the Titan-RT50 contributes to achieving a more stable separation of the droplets. Nevertheless, it possesses certain limitations. In cases where processing parameters are improperly set, the transitional droplets may fail to contact the weld pool within the secondary cur-

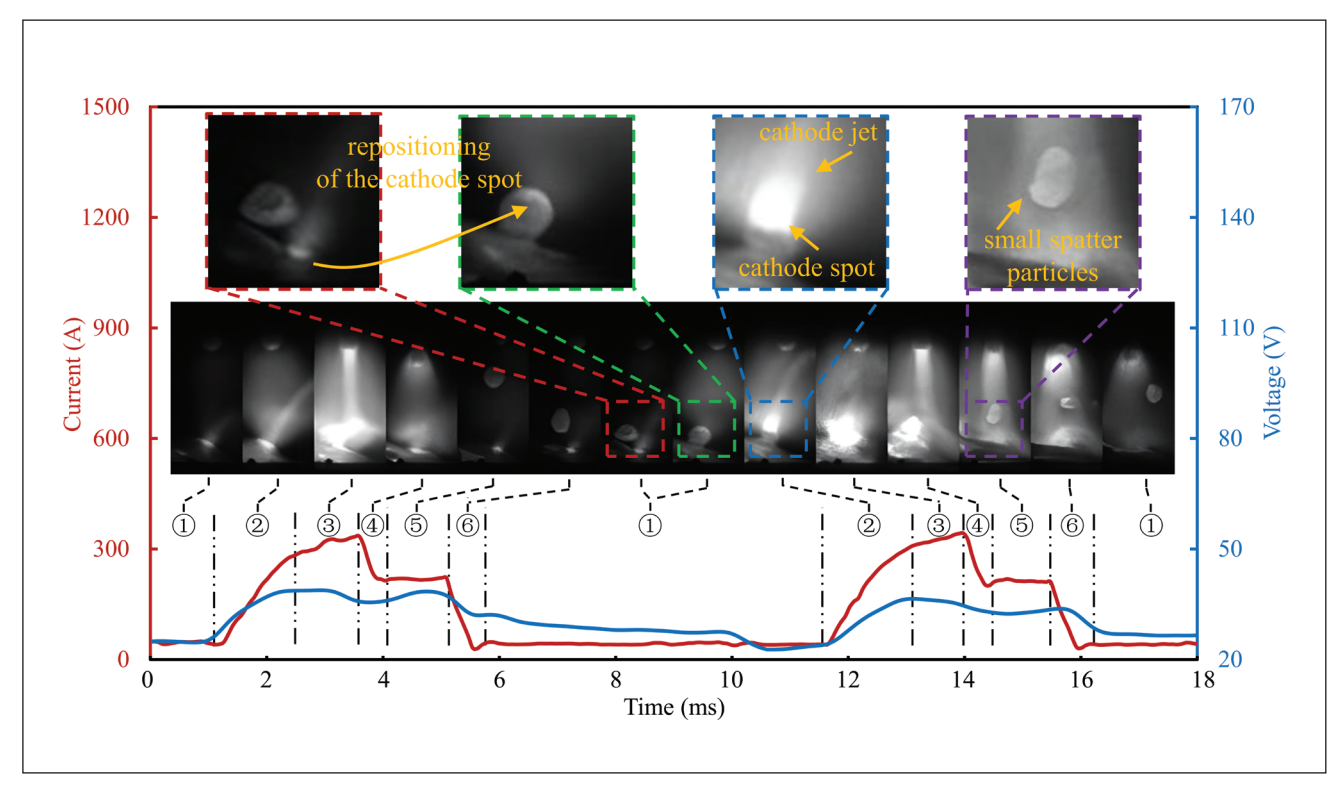


Fig. 4 — The formation process of small spatter particles.

rent-drop stage and base current stage, instead entering the subsequent pulse. This phase mismatch between the droplet transfer behavior and the current waveform inevitably leads to the forceful impingement of the cathode jet on the droplet, thereby causing the occurrence of severe spatter.

This research reveals the existence of two distinct spatter types on the weld surface: small spatter particles with diameters ranging from 0.01 to 0.05 cm (0.004 to 0.020 in.) (as illustrated in Fig. 3A) and large spatter particles with diameters ranging from 0.2 to 0.4 cm (0.079 to 0.157 in.) (as illustrated in Fig. 3B). Through meticulous examination of the high-speed images and synchronous electrical signals captured during the experiments, the formation process of these two spatter types can be comprehensively described as follows.

#### **Small Spatter Particles**

The formation of small spatter particles occurs when the droplet contacts the weld pool, as depicted in Fig. 4. Previous research has extensively investigated this type of spatter, and its formation process can be described as follows (Refs. 9, 11, 12). Due to the sluggish velocity of the droplet, it failed to fully merge with the weld pool and instead proceeded to enter the subsequent pulse. As the arc gradually ignited, the cathode spot repositioned itself from the weld pool to the apex of the droplet, and the cathode jet also reformed at that new origin. Then a portion of the droplet became severed and expelled from the vicinity of the weld pool, ultimately forming the small spatter particles.

#### **Large Spatter Particles**

The formation of large spatter particles takes place before the moment when the droplet contacts the weld pool, specifically during the downward movement of the droplet in the arc space. This spatter has received limited attention, thereby necessitating a detailed description as follows.

The formation process of large spatter particles is depicted in Fig. 5A (with a xenon lamp as the backlight) and Fig. 5B (without a xenon lamp). The current pulses occurring between 1.0 – 6.0 ms and 11.0 – 16.0 ms are denoted as pulse- $\alpha$  and pulse- $\beta$ , respectively, while the corresponding droplets are referred to as droplet- $\alpha$  and droplet- $\beta$ . In the initial stage (0–4.0 ms), droplet- $\alpha$  underwent growth and necking, but contrary to expectations, it failed to fracture during the detachment current stage (4.0-5.0 ms). Instead, the neck fracture occurred within the secondary current-drop stage (5.0–6.0 ms). Then the droplet- $\alpha$  moved at a sluggish transfer velocity and continuously oscillated in the arc space, rendering it incapable of contacting the weld pool during the base current stage (6.0-11.0 ms). Consequently, a considerable distance remained between droplet- $\alpha$  and the weld pool by the time pulse- $\beta$  arrived. Between 11.0-14.0 ms, the arc gradually ignited, and the intense cathode jet associated with pulse-β directly impinged upon droplet- $\alpha$ , causing a significant deflection in its trajectory. This deflection propelled the entire droplet away from the weld pool within the 14.0–16.0 ms interval, ultimately forming the large spatter particles.

The formation of large spatter particles carries significant implications for the stability of the welding process.

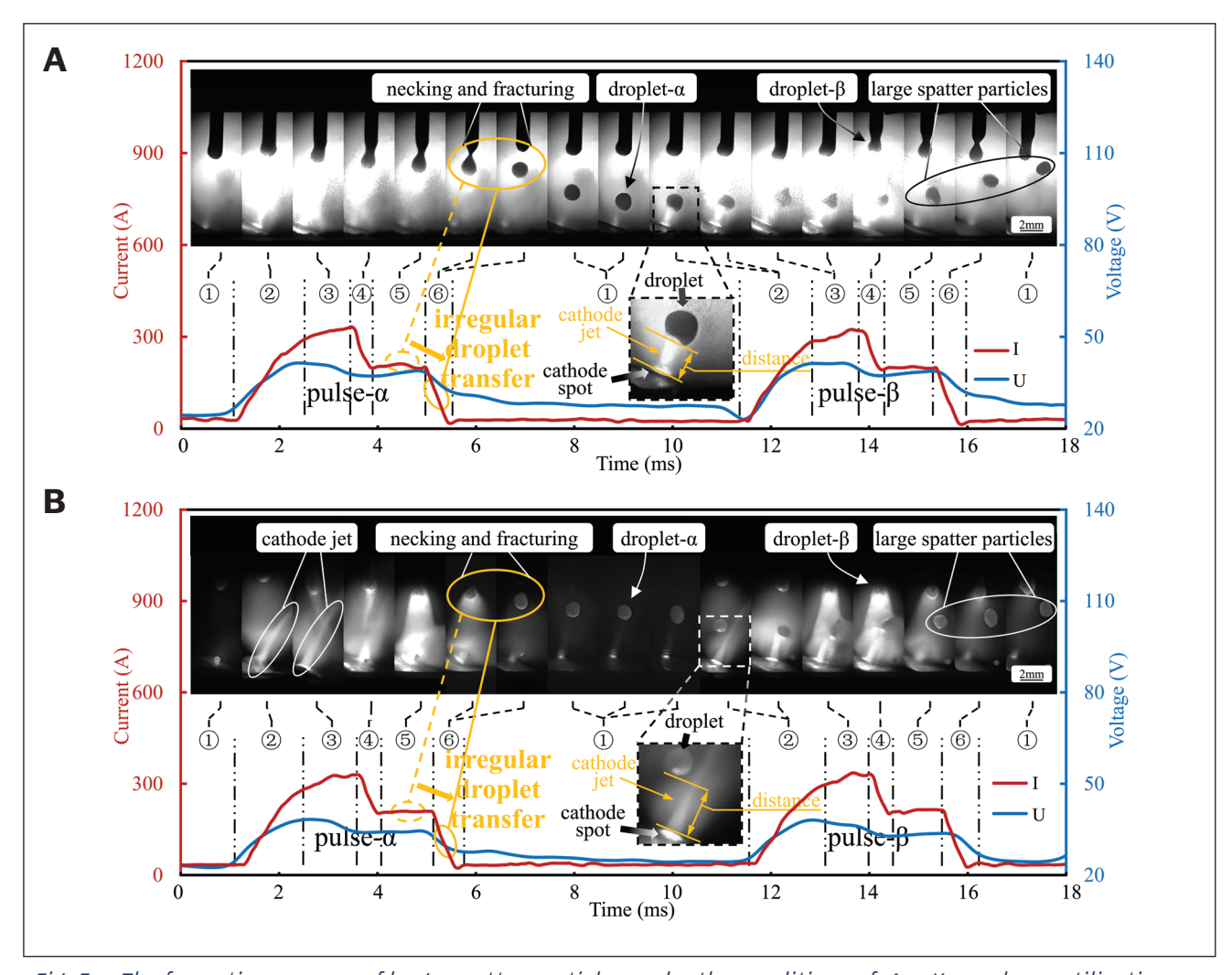


Fig. 5 — The formation process of large spatter particles under the conditions of: A — Xenon lamp utilization; B — non-utilization.

These particles not only hinder the droplet- $\alpha$  from contacting the weld pool but also disrupt the regular transfer of the subsequent 3-4 droplets. It was observed that when droplet- $\alpha$  was subjected to the impingement of pulse- $\beta$ 's cathode jet, the droplet-β, which should transfer regularly, was more likely to experience inadequate necking or even fail to form a neck altogether (as depicted in Figs. 5A and B). In contrast, the current waveform exhibited minimal changes throughout the formation process of large spatter particles, suggesting a relatively stable energy output. This indicated that most of the energy from pulse-β was used to deflect the movement of droplet- $\alpha$  rather than promoting the transfer of droplet-β. Such a phase mismatch between the droplet transfer behavior and the current stage resulted in a highly chaotic transfer process. Moreover, the subsequent 2–3 droplets following droplet-β (not shown) all displayed inconsistent volumes and non-axial transfer to a certain degree, further highlighting the detrimental impact of large spatter particles on the welding process. Therefore, minimizing the formation of large spatter particles is crucial in the GMAW-P process for titanium alloy.

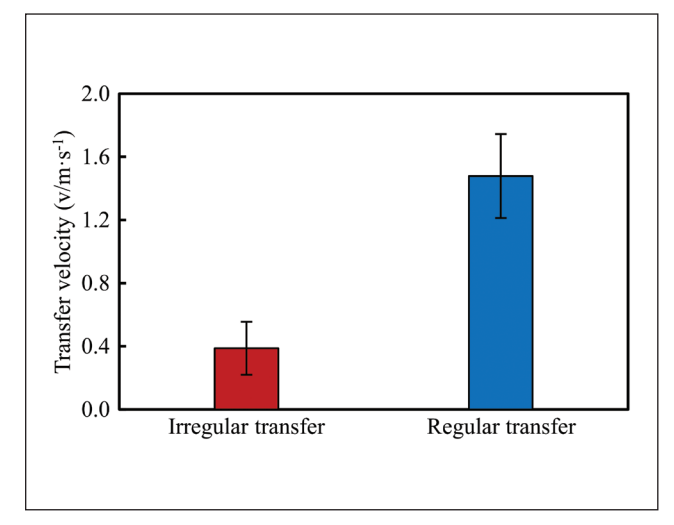


Fig. 6 — The comparison of transfer velocity between regular and irregular transfer.

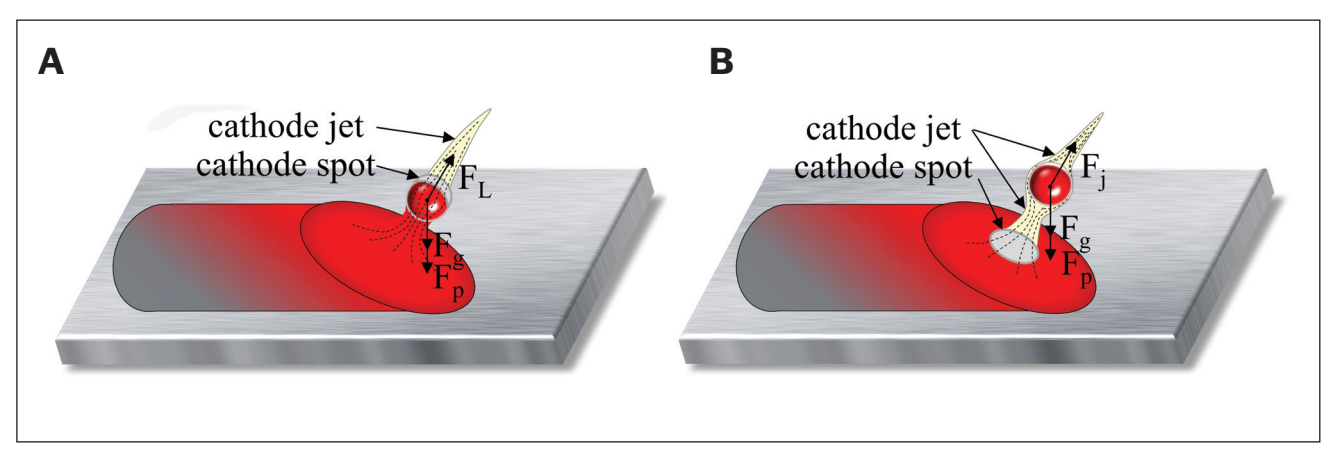


Fig. 7 — The force condition of: A — Small spatter particles; B — large spatter particles.

## **Discussion**

# **Mechanism of Spatter Formation**

To determine the mechanism underlying spatter formation, a meticulous comparative analysis was performed on highspeed images and synchronized electrical signals captured during both regular and irregular droplet transfer processes. The findings revealed that in the regular transfer process, the neck fracture typically occurred during the detachment current stage, whereas the irregular transfer process exhibited a higher likelihood of neck fracture during the secondary current-drop stage (as depicted in Figs. 5A and B). The reduction in current during the secondary current-drop stage resulted in a shift in the dominant force from electromagnetic force to gravity, which played a crucial role in overcoming surface tension and promoting the separation of droplet- $\alpha$ . Consequently, the transfer velocity was considerably slower (as depicted in Fig. 6). Due to this slower velocity (0.4 m/s [1.312 ft/s]), the droplet failed to fully incorporate into the weld pool during the base current stage, causing it to erroneously enter the pulse- $\beta$ . As a result, the intense cathode jet of pulse- $\beta$ led to the formation of both small and large spatter particles.

The electromagnetic force exerted on the droplet is the reason it will form the small spatter particles. The force condition is depicted in Fig. 7A, where the cathode spot is indicated by a silver-gray circular block and the cathode jet is indicated by a beige-striped band. The large current passing through the droplet generates a significant electromagnetic force F, that acts in the opposite direction to gravity  $F_{\alpha}$  and the plasma drag force  $F_{n}$  (a force arising from the high-velocity motion of high-temperature gases). This force condition arises because the electron emission trends take place at higher-temperature regions and the temperature of the droplet is higher than the weld pool. As the transitional droplet contacts the weld pool, the cathode spot will reposition itself to the top of the droplet directionally, leading to the reformation of the cathode jet at a new location. The resulting electromagnetic force then causes the ejection of a portion of the droplet from the vicinity of the weld pool, ultimately forming small spatter particles (Ref. 12).

The cathode jet force exerted on the droplet is the reason it will form the large spatter particles. The force condition is depicted in Fig. 7B. The relatively slow transfer velocity of droplet- $\alpha$  hinders it from contacting the weld pool within the base current stage, as evidenced by the considerable distance observed between droplet- $\alpha$  and the weld pool (as shown in Figs. 5A and B). Pulse-β then arrives and a prominent cathode jet (indicated by a beige-striped band) is formed in the arc space. Since there is no apparent repositioning of the cathode spot (indicated by the silver-gray circular block), droplet- $\alpha$ cannot participate in the electrical circuit, resulting in the absence of the electromagnetic force  $F_i$ . Nevertheless, the intense cathode jet will directly impart momentum to the transitional droplet, leading to the emergence of a strong cathode jet force F, that impedes the droplet transfer. When the accumulated momentum of resultant force (i.e., cathode jet force F, gravity F, and plasma drag force F, surpasses the downward momentum of the droplet, the entire droplet will be deflected at a significant angle and moves away from the weld pool, ultimately giving rise to the formation of large spatter particles.

To date, previous studies have predominantly focused on the formation of small spatter particles occurring when the droplet contacts the weld pool (Refs. 9, 11, 12). However, limited attention has been given to the detailed analysis of large spatter particles formed during the droplet's downward movement in the arc space. This knowledge gap stems from the inherent disparities between direct current (DC) welding and pulsed current welding. In DC welding with low current, although the transfer velocity is sluggish, the cathode jet force which is directly related to the current magnitude, also remains relatively small. The upward momentum of the resultant force is insufficient to surpass the downward momentum of the droplet, precluding the formation of large spatter particles. Similarly, in DC welding with high current, despite the substantial increase in the cathode jet force, the transfer velocity increases with larger amplitude, thus still mitigating the likelihood of large spatter particle formation. Unfortunately, pulsed current welding presents an inherent potential for the occurrence of large spatter particles. The necking fracture of droplet-α may inadvertently transpire during the secondary current-drop stage (50-200 A), resulting in a transfer velocity akin to that observed in low-current

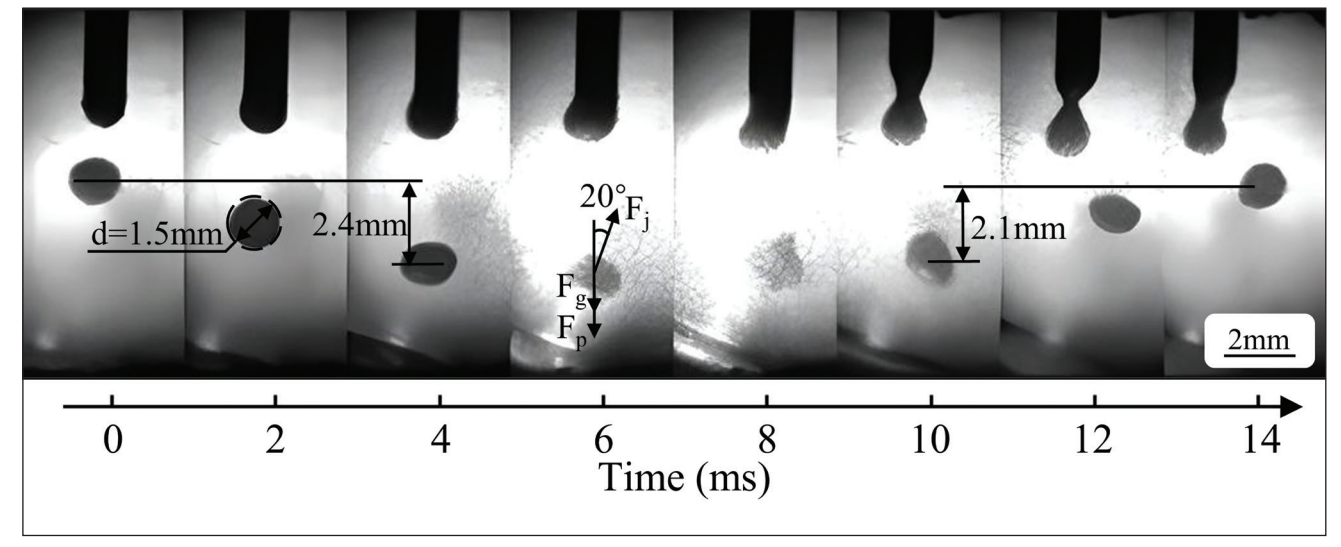


Fig. 8 — The physical parameters required for the force analysis.

DC welding. When droplet- $\alpha$  erroneously enters the pulsing current stage (200–350 A), the intensity of the cathode jet becomes comparable to that experienced in high-current DC welding. Consequently, the upward momentum of the resultant force may surpass the downward momentum of the droplet, ultimately leading to the formation of large spatter particles.

## **Force Analysis of Droplets**

Following the qualitative examination of the formation of large spatter particles, a quantitative analysis of the forces exerted on the droplets can offer deeper insights into the effect of the cathode jet, despite the inherently rough nature of force analysis. In this study, the modified static force balance theory (Ref. 20) is utilized to conduct the force analysis, aiming to assess three distinct forces: the gravity  $F_{g}$  and plasma drag force  $F_{g}$  acting as promoting forces, and the cathode jet force Facting as a resisting force. Note that the analysis excludes the consideration of the electromagnetic force F, due to the absence of current flowing through the droplet during the formation process of large spatter particles. Regarding the physical parameters necessary for the force analysis, we have calculated a total of seven sets of values during data processing. These seven sets of values exhibit minimal errors. Hence, we opt to utilize a representative set of data to conduct subsequent force analysis. The pertinent physical parameters we opted are presented in Fig. 8. The current waveform depicted in Fig. 5A can be fit by a polynomial function as follows:

$$I(t) = 0.412t^6 - 9.35t^5 + 74.6t^4$$
$$-263t^3 + 359t^2 - 3t + 49, t \in (0,5ms)$$
 (1)

For gravity, assuming the droplet to be a standard sphere, the density of titanium is established at  $4.42 \, g \, (0.156 \, oz) / \, cm3$  (Ref. 21), and the diameter of the droplet is measured

to be 1.5 mm (0.059 in.). With these parameters in place, the gravity can be calculated by applying the equation:

$$F_g = \pi d^3 \rho g / 6 = 7.7 \times 10^{-5} N \tag{2}$$

where g is the gravitational acceleration.

For the plasma drag force, it can be given as follows (Ref. 20):

$$F_p = C_D A_p \rho_f v_f^2 / 2 \tag{3}$$

where  $C_{\scriptscriptstyle D}$  is the dimensionless drag coefficient (taking 0.44 [Ref. 22]),  $A_{\scriptscriptstyle P}$  is the projected area perpendicular to fluid flow (taking 1.8 × 10<sup>-6</sup> m²),  $\rho_{\scriptscriptstyle f}$  is the density of arc plasma (taking 0.04 kg/m³ [0.0089 lb]) (Ref. 12), and  $v_{\scriptscriptstyle f}$  is the velocity of arc plasma around the droplet. When conducting the force analysis on a specific droplet under a fixed welding process, other parameters (i.e.,  $C_{\scriptscriptstyle D}$ ,  $A_{\scriptscriptstyle P}$ , and  $\rho_{\scriptscriptstyle f}$ ) are held constant, while the  $v_{\scriptscriptstyle f}$  is proportional to the varying current within a single pulse cycle (Ref. 23). Hence, the plasma drag force exhibits a quadratic relationship with the welding current.

The  $v_f$  reaches a value of 100 m (328.084 ft)/s when it reaches the pulsing current stage (Ref. 20), so the maximum plasma drag force can be calculated to be 1.6  $\times$  10<sup>-4</sup> N. Since the welding current ranges from 50 A to 350 A in this study, the plasma drag force can be calculated from

$$F_p(t) = 1.3 \times 10^{-9} I^2(t)$$
 (4)

For the cathode jet force, it can be given as follows (Ref. 20):

$$F_j = \frac{\mu_0 I^2}{8\pi} \tag{5}$$

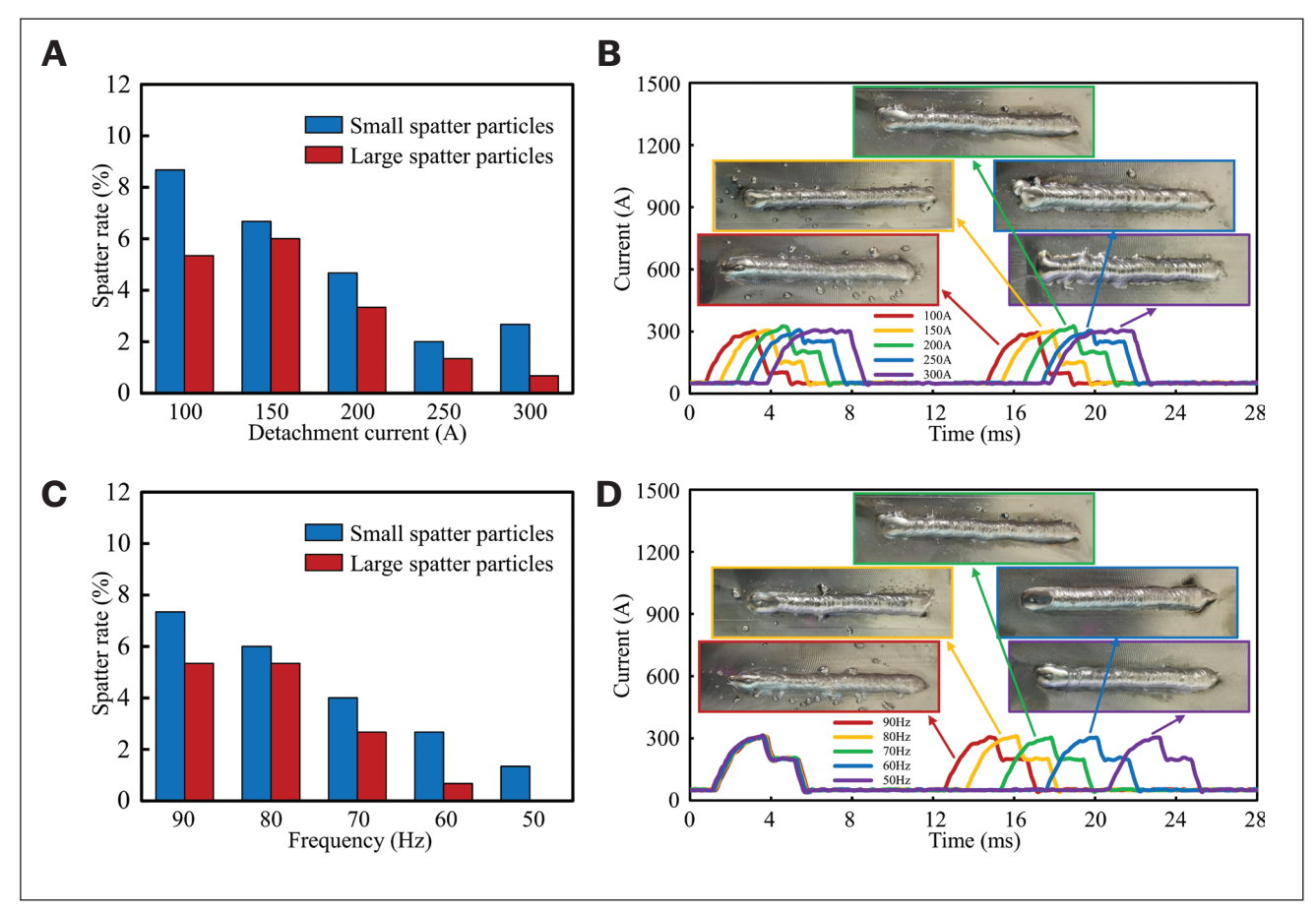


Fig.  $9 - A - Spatter\ rate$ ;  $B - bead\ formation\ exhibiting\ variations\ corresponding\ to\ changes\ in\ detachment$ current, while maintaining a fixed pulsing frequency of 70 Hz. C — spatter rate; D — bead formation exhibiting variations in response to adjustments in the pulsing frequency, with a fixed detachment current of 200 A.

where  $\mu_0$  is the permeability of free space (taking  $4\pi \times 10^{-7}$ N/A<sup>2</sup>). Therefore, the cathode jet force can be calculated by applying the equation:

$$F_j(t) = 0.5 \times 10^{-7} I^2(t)$$
 (6)

Based on equations 2, 4, and 6, it can be observed that the cathode jet force is 38 times that of the plasma drag force, with gravity being negligible. Driven by the resultant force mainly comprised of the cathode jet force, the droplet undergoes a rapid deceleration followed by a reversed acceleration within a very short time span. This intricate process can be effectively analyzed by using the momentum theorem.

For the downward momentum of droplet, the droplet prior to the impact of the cathode jet exhibits a transfer velocity of approximately 0.6 m (1.968 ft)/s in the vertically downward direction, while the velocity after the impact is 0.53 m (1.739 ft)/s with the direction being perpendicular to the weld pool (calculated based on the information provided by Fig. 8, corresponding to displacements of 2.4 mm [0.094 in.] and 2.1 mm [0.083 in.] within the respective 4 ms intervals). Considering the mass of the droplet as  $7.7 \times 10^{-3}$  g and the inclination of the weld pool at approximately 20 deg from the horizontal, the alteration in droplet momentum can be calculated from

$$m\Delta v = 7.7 \times 10^{-3} g \times \frac{1.11m}{m}$$
  
= 8.55 × 10<sup>-6</sup>kg ·  $\frac{m}{s}$  (7)

For the upward momentum of resultant force, the resultant force can be calculated by applying the equation:

$$F_r(t) = F_f(t) - F_p(t) - F_g = (0.085t^{12} - 3.854t^{11} + 74.469t^{10} - 806.06t^9 + 5390.1t^8 - 22974.2t^7 + 61638.6t^6 - (8)$$

$$94977t^5 + 68495t^4 - 12854t^3 + 16168t^2 - 126t + 226) \times 10^{-7}N$$

Within a single pulse duration, specifically a 5-millisecond interval, the upward momentum resulting from the combined forces can be determined by evaluating the equation:

$$Ft = \int_0^5 F_r(t)dt = 1.04 \times 10^{-5} \, N \cdot s \tag{9}$$

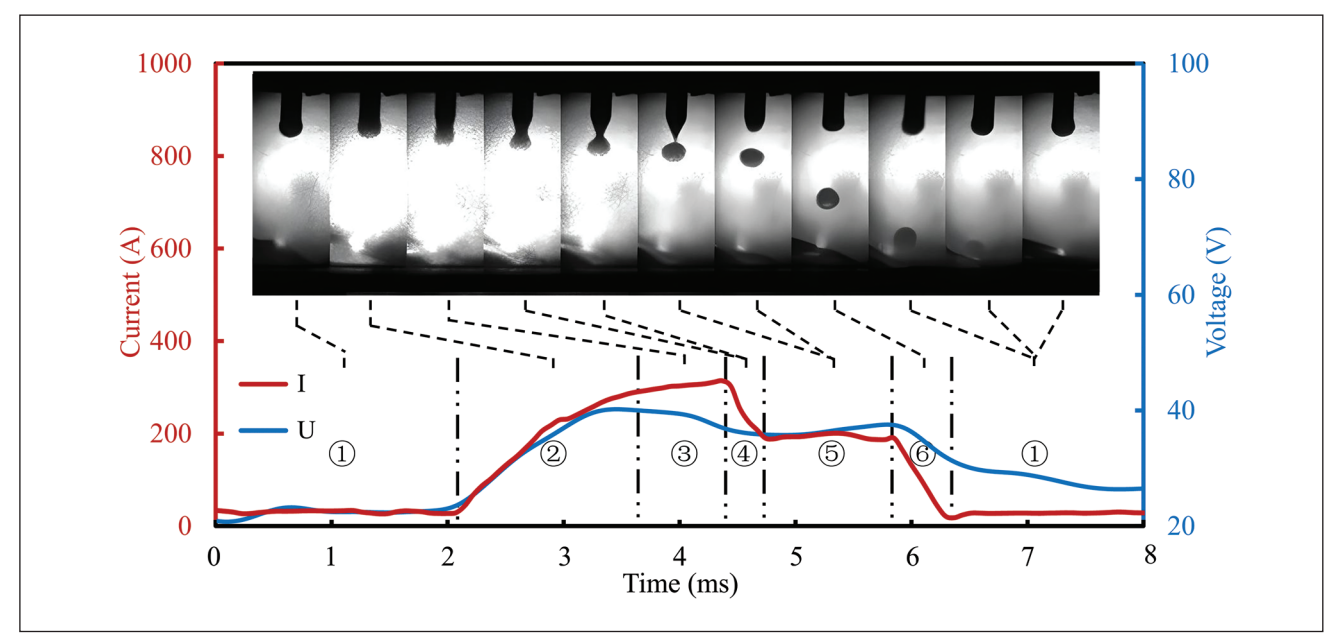


Fig. 10 — The desirable droplet transfer behavior in different current stages.

The upward momentum generated by the resultant force within a single pulse duration is found to be 1.22 times the change in downward momentum of the droplet. It is worth noting that this value can be further approximated to 1 by considering the introduction of an energy loss coefficient. The quantitative analysis provides further confirmation that the cathode jet force is indeed responsible for the formation of large spatter particles.

# **Strategies to Suppress Spatter**

According to the analysis, the causal chain leading to spatter formation can be elucidated as follows: the inadvertent occurrence of neck fracture in the secondary current-drop stage induces a comparatively sluggish transfer velocity, subsequently causing the droplet- $\alpha$  to erroneously enter the pulse-β, ultimately culminating in spatter formation propelled by the cathode jet. Therefore, two ideas can be considered to suppress spatter. On the one hand, addressing the fundamental issue, the neck fracture should take place during the detachment current stage to circumvent the sluggish transfer velocity. On the other hand, from a procedural standpoint, droplets with reduced transfer velocity should be afforded ample time to complete the transfer process without entering the pulse- $\beta$  erroneously. The corresponding strategies for these two ideas involve increasing the detachment current and decreasing the pulse frequency, respectively.

As depicted in Fig. 9A, with a fixed pulsing frequency of 70 Hz and an increase in detachment current from 100 A to 300 A, the rate of small spatter particles decreased from 8.67% to 2.67%, while the rate of large spatter particles decreased from 5.33% to 0.67%. Figure 9B verified the associated enhancement in bead formation as the detachment current increased, with the only drawback being a slight waviness observed when the detachment current exceeded 200 A. This waviness could potentially be attributed to the

instability of the weld pool caused by the excessively high transfer velocities of molten droplets.

Similarly, as shown in Fig. 9C, with a fixed detachment current of 200 A and a decrease in pulsing frequency from 90 Hz to 50 Hz, the rate of small spatter particles decreased from 7.33% to 1.33%, while the rate of large spatter particles decreased from 5.33% to 0%. Figure 9D validated the corresponding improvement in bead formation achieved by reducing the pulsing frequency, albeit at the expense of welding efficiency.

Note that the occurrence rate of large spatter particles is typically lower than that of small spatter particles, as the former necessitates more stringent conditions for formation, namely lower transfer velocities. Fig. 10 exhibits a desirable transfer process characterized by the absence of spatter formation, achieved by configuring the detachment current and pulsing frequency to 200 A and 60 Hz, respectively. This configuration ensures that the transitional droplets can be fully incorporated into the pool within the base current stage, effectively circumventing the detrimental influence of the cathode jet.

#### **Conclusions**

In the GMAW-P process for titanium alloy, both large and small spatter particles may generate due to the intensive spurt of the cathode jet from a relatively fixed cathode spot. To effectively suppress spatter, two simple yet efficacious strategies have been identified: increasing the detachment current and decreasing the pulsing frequency. The key findings of this research can be summarized as follows:

1. The large spatter particles originate from the whole transitional molten droplet as it descends within the arc space, while the small spatter particles are formed by the partial transitional molten droplet as it makes contact with the weld

- pool. The cathode jet force accounts for the formation of large spatter particles, whereas the electromagnetic force is responsible for the small spatter particles.
- 2. The relatively slow transfer velocities contribute to the impingement of the cathode jet on droplets. During the formation process of large spatter particles, the cathode jet force is 38 times the plasma drag force with gravity being negligible. Under the detrimental effect of cathode jet force, the droplet velocity undergoes a deflection from a vertical downward direction (approximately 0.6 m/s) to an oblique upward direction (approximately 0.53 m/s).
- 3. By increasing the detachment current and decreasing the pulsing frequency, the spatter formation can be effectively suppressed. The spatter rate decreases from 14.00% to 3.33% with an increase in detachment current from 100 A to 300 A, and decreases from 12.67% to 1.33% with a decrease in pulsing frequency from 90 Hz to 50 Hz.

#### **Acknowledgments**

This program was supported by the National Natural Science Foundation of China (Grant No. 52005366), Natural Science Foundation of Tianjin (Grant No. 21JCQNJC00570), State Key Laboratory of Advanced Welding and Joining, Harbin Institute of Technology (Grant No. AWJ21M12).

#### References

- 1. Boyer, R. R. 1996. An overview on the use of titanium in the aerospace industry. *Materials Science and Engineering A* 213(1–2): 103-114.
- 2. Takahashi, K., Mori, K., and Takebe, H. 2020. Application of titanium and its alloys for automobile parts. In MATEC web of conferences 321: 02003. EDP Sciences.
- 3. Ali, A., Pan, L., Duan, L., Zheng, Z., and Sapkota, B. 2016. Characterization of seawater hygrothermal conditioning effects on the properties of titanium-based fiber-metal laminates for marine applications. Composite Structures 158: 199–207.
- 4. Zhang, Y. M., and Zhang, S. B. 1999. Observation of the keyhole during plasma arc welding. Welding Journal 78: 53-s.
- 5. Li, X. R., Shao, Z., and Zhang, Y. M. 2012. Double stage plasma arc pipe welding process. Welding Journal 91: 346-353.
- 6. Pardal, G., Martina, F., and Williams, S. 2019. Laser stabilization of GMAW additive manufacturing of Ti-6Al-4V components. Journal of Materials Processing Technology 272: 1–8.
- 7. Choudhury, S. S., Marya, S. K., and Amirthalingam, M. 2021. Improving arc stability during wire arc additive manufacturing of thin-walled titanium components. Journal of Manufacturing Processes 66: 53-69.
- 8. Zhang, Y., Cheng, F., and Wu, S. 2021. The microstructure and mechanical properties of duplex stainless steel components fabricated via flux-cored wire arc-additive manufacturing. Journal of Manufacturing Processes 69: 204-214.
- 9. Shinn, B. W., Farson, D. F., and Denney, P. E. 2005. Laser stabilisation of arc cathode spots in titanium welding. Science and Technology of welding and Joining 10(4): 475-481.
- 10. Lee, T. H., Kam, D. H., Oh, J. H., and Kim, C. 2022. Ti-6Al-4V alloy deposition characteristics at electrode-negative polarity in the cold metal transfer-gas metal arc process. Journal of Materials Research and Technology 19: 685-696.
- 11. Lee, T. H., Kim, C., Oh, J. H., and Kam, D. H. 2022. Visualization of cathode spot control using laser irradiation and oxide addition in

- wire arc additive manufacturing of titanium alloys. Journal of Laser Applications 34(4): 042024.
- 12. Eickhoff, S. T., and Eagar, T. W. 1990. Characterization of spatter in low-current GMAW of titanium alloy plate. Welding Journal
- 13. Denney, P. E., Shinn, B. W., and Fallara, P. M. 2005. Laser Plus GMAW Hybrid Welding of Titanium. In The Fifteenth International Offshore and Polar Engineering Conference. OnePetro.
- 14. Li, C., Muneharua, K., Takao, S., and Kouji, H. 2009. Fiber laser-GMA hybrid welding of commercially pure titanium. Materials & Design 30(1): 109-114.
- 15. Denney, P. E., Shinn, B. W., and Fallara, P. M. 2004. Stabilization of pulsed GMAW in titanium welds with low-power lasers. In International Congress on Applications of Lasers & Electro-Optics 2004(1): 202. Laser Institute of America.
- 16. Zhang, Y. M., and Li, P. J. 2001. Modified active control of metal transfer and pulsed GMAW of titanium. Welding Journal 80(2): 54.
- 17. Sun, Z., Lv, Y., Xu, B., Liu, Y., Lin, J., and Wang, K. 2015. Investigation of droplet transfer behaviours in cold metal transfer (CMT) process on welding Ti-6Al-4V alloy. The International Journal of Advanced Manufacturing Technology 80: 2007-2014.
- 18. Zhou, S., Xie, H., Ni, J., Yang, G., Qin, L., and Guo, X. 2022. Metal transfer behavior during CMT-based Wire Arc Additive Manufacturing of Ti-6Al-4V alloy. Journal of Manufacturing Processes 82:159-173.
- 19. Lee, T. H., Kang, M., Oh, J. H., and Kam, D. H. 2022. Deposition quality and efficiency improvement method for additive manufacturing of Ti-6Al-4V using gas metal arc with CMT. Journal of Materials Processing Technology 308: 117720.
- 20. Kim, Y. S., and Eagar, T. W. 1993. Analysis of metal transfer in gas metal arc welding. Welding Journal 72: 269-s.
- 21. Boivineau, M., Cagran, C., Doytier, D., Eyraud, V., Nadal, M. H., Wilthan, B., and Pottlacher, G. 2006. Thermophysical properties of solid and liquid Ti-6Al-4V (TA6V) alloy. International journal of thermophysics 27: 507-529.
- 22. Zhang, X., Gao, H., and Li, Z. 2021. Forces analysis of droplets and accurate control of metal transfer in GMAW by utilizing droplet resonance. Journal of Manufacturing Processes 70: 121–131.
- 23. Li, K., Wu, Z., and Liu, C. 2015. Measurement and calculation of plasma drag force in arc welding based on high-speed photography technology and particle dynamics. *Materials & Design* 85: 97–101.

ZHENDAN ZHENG, SHAOJIE WU, LIMIN FAN, HAO WU, and FANGJIE CHENG are with the School of Materials Science and Engineering, Tianjin University, Tianjin, China. SHAOJIE WU is also with the State Key Laboratory of Advanced Welding and Joining, Harbin Institute of Technology, Harbin, China. SHAOJIE WU and CHENG are also with the Tianjin Key Laboratory of Advanced Joining Technology, Tianjin, China.